



Thermophysical property prediction of biodiesel mixtures at extreme conditions using molecular dynamics simulation



Cheng Chen^a, Daniel Mira^b, Zhihao Xing^a, Xi Jiang^{a,*}

^a School of Engineering and Materials Science, Queen Mary University of London, Mile End Road, London E1 4NS, UK

^b Barcelona Supercomputing Center (BSC), Plaça Eusebi Güell, 1-3, Barcelona, Spain

ARTICLE INFO

Article history:

Received 9 July 2022

Revised 6 September 2022

Accepted 18 September 2022

Available online 01 October 2022

Keywords:

Biodiesel

Thermophysical property

Supercritical conditions

Molecular dynamics

ABSTRACT

Liquid biofuels such as biodiesel are playing an increasing role in renewable energy utilisation, but accurate predictions of fuel properties at extreme conditions remain challenging. In this study, molecular dynamics (MD) simulation with classical force field is performed to obtain the thermophysical properties of biodiesel over extended ranges of temperatures and pressures. The predicted properties include the critical temperature, critical density, critical pressure, surface tension, viscosity, thermal conductivity and diffusion coefficient. The specific MD setup for fuel thermophysical property prediction is examined. It is observed that the long-range dispersion interaction is essential to accurately predicting the surface tension, and averaging over a sufficient number of independent replication simulations is required to eliminate the statistical error when using the Green-Kubo method for viscosity calculation. The reliability of MD approach is validated against experimental data at normal temperature and pressure. The equilibrium MD simulation has an advantage over nonequilibrium MD simulation when building databases of fuel properties. Moreover, the properties of biodiesel are compared with conventional diesel to elucidate the effects of fuel composition and molecular structure of the fuel surrogates on fuel thermophysical properties. For biodiesel utilisation, higher values of critical temperature, surface tension and viscosity, lower diffusivity together with the increased aggregation tendency in bath gas indicate the needs of further optimisation of injection system to achieve the desired mixing in combustion applications.

© 2022 The Author(s). Published by Elsevier B.V. This is an open access article under the CC BY-NC license (<http://creativecommons.org/licenses/by-nc/4.0/>).

1. Background

It is a consensus that liquid fuel vehicles will continue to be used for many decades particularly in the long-haul road freight transport and marine transport for international trading, even when electric vehicles are expected to become dominant for passenger cars in the global automotive market. In spite of the encouraging expectation in electrification of light-duty passenger vehicles, liquid fuels still provide over 50% of transportation energy [1–3], and there is little near future prospect for battery-powered jetliners, heavy goods vehicles and marine vessels. Biodiesel and bioethanol are currently two of the commercially available large-scale sustainable biofuels that can be produced from a variety of resources. Neat biodiesel or biodiesel/diesel blended fuels can be employed in current diesel engine infrastructure without major modifications to the engine, taking advantages of its low sulphur and aromatic contents and the substantial decrease in CO emission.

With the ever-pressing needs of cleaner and more efficient fuel utilisation, combustion engine systems tend to operate at increasingly higher pressure. Injectors with common rail system pump fuels at extremely high pressure, usually above 200 MPa, meaning that fuel viscosity increases substantially over the atmospheric value. Recent observation of the crystallisation and solidification process of rapeseed oil methyl esters at high pressure above 230 MPa highlights the challenges in understanding the rheological property of biodiesel in nozzles [4]. The next generation engine combustors will operate at considerably higher pressure of around 100 bar, which is above the fuel critical point, *i.e.*, at supercritical conditions. The engine injection is thereby described as a transcritical process with subcritical liquid fuel under extremely high pressure injected into supercritical ambient gases. The fuel jet can be heated to a supercritical temperature before combustion takes place. In such conditions, surface tension diminishes, and distinct liquid and gas phases do not exist. It is known that high-temperature and high-pressure (HTHP) supercritical fuels have properties of lower density, viscosity and higher diffusivity which are beneficial for achieving high quality fuel/air mixing.

* Corresponding author.

E-mail address: xi.jiang@qmul.ac.uk (X. Jiang).

Prediction of fluid behaviour at HTHP supercritical conditions still remains a fundamental challenge. It requires new theoretical methods particularly considering the phase transition between “rigid-like”, “liquid-like” and “gas-like” due to the existence of Frenkel line or Widom line [5]. Directly measuring physical properties for every encountered fluid at all conditions of interest is not only expensive and time-consuming but also extremely difficult and sometimes impossible. Due to the variety of feedstock sources for biodiesel production, this renewable liquid fuel has varying compositions. In comparison with conventional diesel fuels comprised of alkanes, aromatics and even sulfur, the contents of biodiesel are primarily fatty acid methyl esters (FAMES) with different chain lengths and unsaturation degrees [6,7]. It has been reported widely that the oxygen atoms in FAME molecules lead to substantial reduction in emissions of particulate matter, total hydrocarbons and carbon monoxide, while the power loss is imperceptible in unmodified conventional engines when biodiesel is used [8]. Understanding the relations between biodiesel composition and its physicochemical properties is essential to fuel quality evaluation, storage and development of cleaner and more efficient engines.

Most data available in the literature encompasses the temperature dependence of biodiesel at atmospheric pressure. Fewer studies (actually only seven studies were mentioned in the latest review of Abel *et al.* [9]) have dedicated to measuring and predicting the properties of fuel mixtures in HTHP conditions. As a computer simulation method for analysing the physical movements of atoms and molecules, MD has also been successfully used to predict the thermophysical properties (density, enthalpy of vaporization, heat capacity, surface tension, isothermal compressibility, *etc.*) of organics like alkane, aromatics, methyl esters, alcohols, water, ionic liquids, crude oil, *etc.* [10]. For example, after reviewing the application of MD on calculating transport properties of working fluids at supercritical conditions, Nie *et al.* [11] concluded that MD can be considered as an effective tool. Using equilibrium molecular dynamics (EMD), Yang *et al.* [12,13] predicted the viscosity and thermal conductivity of liquid aviation fuels, which include trimethylbenzene, *n*-decane, *n*-dodecane and their mixtures in sub/supercritical conditions. The results showed good agreements with the NIST data. The advantage of EMD is its flexibility at different conditions to calculate a variety of transport properties such as self-diffusion coefficient, shear viscosity and thermal conductivity *etc.*, from the basic molecular properties such as the molecular coordination, velocity, pressure tensor and kinetic energy. Accurate prediction of the vapour-liquid equilibrium (VLE) and vapour-liquid interfacial tension of hydrocarbons and their mixtures was also achieved in the work of Morrow *et al.* [14]. Chae *et al.* [15,16] quantified the effect of molecular structure of alkane

isomers on mutual diffusion coefficient in N₂. Recently, Oliveira *et al.* [17] studied the molecular arrangement in diesel/biodiesel blends and the impact of biodiesel as an additive on the stabilization of diesel/ethanol blends. Molecular dynamics simulation has also been used to study the complex phenomena of multicomponent fuel droplet evaporation in sub- to supercritical conditions [18,19]. It is expected that MD modelling becomes routinely used to provide the fundamental knowledge and physical insight for the practical use of liquid fuels, considering that force fields and molecular simulation are more and more accurate and affordable.

In this study, MD simulation is employed to deal with the challenges of biodiesel thermophysical property prediction. This study was oriented to addressing a number of specific issues in three areas where there is currently a lack of understanding or reliable predictive methods, including (1) critical property and surface tension prediction of fuel mixtures; (2) calculation of transport properties such as density, viscosity, thermal conductivity, and diffusivity of the fuel mixtures in a wide range of conditions; and (3) elucidating the effects of molecular structure on thermophysical properties. The paper is organised into a few sections. Section 2 presents the specific methodological approaches and MD setup. Section 3 is devoted to present the EMD simulation results of biodiesel mixtures and the comparison with conventional diesel. The subsequent section is set to evaluate the feasibility of using nonequilibrium MD (NEMD) simulations in thermophysical property prediction at extreme conditions. Finally, conclusions from the study are drawn.

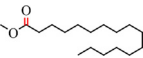
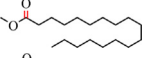
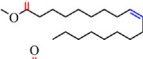
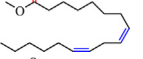
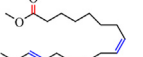
2. Models and methodology

2.1. Composition and molecular structures

For biodiesel, the dominant commercial feedstocks in USA, Europe, and southeast Asia are soybean, rapeseed and palm respectively. Although considerable composition variability exists across biodiesel fuels produced from different feedstocks, the majority is dominated by five fatty acid species with varying molecular chain lengths and unsaturation degrees, *i.e.*, palmitic (16:0), stearic (18:0), oleic (18:1), linoleic (18:2), and linolenic (18:3). In this study, the rapeseed biodiesel is selected as the research object with the molecular structure and composition adopted from the work of Herbinet *et al.* [20]. The details are listed in Table 1.

Different from biodiesel, commercial diesel contains hundreds of different hydrocarbons, and the mixture is too complex to be modelled accurately. The combination of several representative fuel components in a surrogate model to emulate most important properties of real commercial diesel is a common strategy. A

Table 1
Chemical compound names, chemical formulas, molecular structures, molecular weights and composition of biodiesel.

Common Name	Molecular Formula	Molecular Structure	Molecular Weight (g/mol)	Composition (mol %)
Methyl Palmitate	MP (C16:0) C ₁₇ H ₃₄ O ₂		270.46	4.3
Methyl Stearate	MS (C18:0) C ₁₉ H ₃₈ O ₂		298.51	1.3
cis-9-Methyl Oleate	MO (C18:1) C ₁₉ H ₃₆ O ₂		296.50	59.9
cis-9,12-Methyl Linoleic	ML (C18:2) C ₁₉ H ₃₄ O ₂		294.48	21.1
cis-9,12,15-Methyl Linolenate	MLN (C18:3) C ₁₉ H ₃₂ O ₂		292.47	13.2

recently developed five-component diesel surrogate fuel by Qian et al. [21] is employed in this study, in order to facilitate the definition of fuel mixture properties with high similarity to real fuels. The composition and molecular structures are listed in Table 2.

2.2. Thermophysical property calculation and simulation details

2.2.1. Classical force field

The Transferable Potentials for Phase Equilibria - united atom (TraPPE-UA) force field [22] is employed in this study to calculate the physical properties of the liquid fuels. TraPPE force field is developed for the simulation of phase equilibrium in which carbon and bonded hydrogen atoms are treated as a “pseudo-atom” for computational efficiency. It has been used widely to predict the density, surface tension, viscosity, thermal conductivity and diffusion of linear alkanes, cycloalkanes, aromatics and biofuels having function groups of methyl esters [12,14,23,24].

The overall energy of the MD system can be described as:

$$E = E_{\text{bond}} + E_{\text{angle}} + E_{\text{dihedral}} + E_{\text{improper}} + E_{\text{vdW}} + E_{\text{Coul}} \quad (1)$$

where the first four terms on the right-hand side refer to intramolecular contributions to the total energy, i.e., bond stretching, angle bending, dihedral and improper dihedral. The last two terms describe the non-bonded interaction including van der Waals (vdW) interactions and the Coulomb interactions:

$$E_{\text{nb}}(r_{ij}) = 4\epsilon_{ij} \left(\left(\frac{\sigma_{ij}}{r_{ij}} \right)^{12} - \left(\frac{\sigma_{ij}}{r_{ij}} \right)^6 \right) + \frac{q_i q_j}{4\pi\epsilon_0 r_{ij}} \quad (2)$$

where r_{ij} , σ_{ij} , ϵ_{ij} , q_i , and q_j are the separation distance between integration sites i and j , the Lennard-Jones (LJ) diameter and well depth, and the partial charges on interaction sites i and j , respectively. ϵ_0 is the vacuum permittivity. Intramolecular 1–4 LJ and Coulomb interactions are excluded. The parameters for the unlike interactions are computed using Lorentz-Berthelot combining rules expressed as:

$$\sigma_{ij} = \frac{1}{2} (\sigma_{ii} + \sigma_{jj}), \epsilon_{ij} = \sqrt{\epsilon_{ii}\epsilon_{jj}} \quad (3)$$

2.2.2. Basic MD setup

In this study, all the simulations are performed using the code Large-scale Atomic/Molecular Massively Parallel Simulator (LAMMPS) [25]. Three types of ensembles are considered for different scenarios, i.e., *NPT* (constant number of atoms, pressure, and temperature), *NVT* (constant number of atoms, volume, and temperature) and *NVE* (microcanonical ensemble). The Nose-Hoover thermostat and barostat are used to control the temperature and pressure with the damping constants equal to 100 and 1000 times of the time step respectively. The cut-off distance of the vdW interactions and Coulomb interactions are set to be 1.4 nm. The

particle-particle particle-mesh (PPPM) solver is used for the calculation of long-range electrostatic interactions in reciprocal space with the desired relative force error of $1e-4$. All simulations were performed with initial energy minimisation before the equilibrium and production runs. Periodic boundary conditions are used in all directions of the computational domain. Time step in production run is set at 1 fs. All simulations are performed five times separately to avoid statistical error with initial velocities randomly set following a Gaussian distribution. Visualization and data post processing is performed in OVITO (The Open Visualization Tool) [26].

2.2.3. Density, viscosity and thermal conductivity

Density can be directly obtained by averaging results over the last 1 ns trajectories after sufficiently equilibrated *NPT* runs. In general, viscosity and thermal conductivity can be calculated using the Green-Kubo (GK) method in EMD simulation. For viscosity (η), it can be expressed as the time integration of the auto correlation function (ACF, also indicated as $C(t)$) of the pressure tensor:

$$\eta = \frac{V}{3k_B T} \int_0^\infty \langle (\sum_{\alpha\beta} P_{\alpha\beta}(0) \cdot P_{\alpha\beta}(t)) \rangle dt \quad (4)$$

where α and β represent any pair of distinct Cartesian coordinates x , y , and z , $P_{\alpha\beta}$ are off-diagonal components of the pressure tensor, V and T are system volume and temperature, k_B is Boltzmann constant equals to $1.380649 \times 10^{-23} \text{ J}\cdot\text{K}^{-1}$, and $\langle \dots \rangle$ is used to represent an average over the ensemble.

The thermal conductivity (κ) using GK method is expressed as the time integration of the ACF of the heat flux:

$$\kappa = \frac{V}{k_B T^2} \int_0^\infty \langle q_x(0) \cdot q_x(t) \rangle dt = \frac{V}{3k_B T^2} \int_0^\infty \langle \mathbf{q}(0) \cdot \mathbf{q}(t) \rangle dt \quad (5)$$

where \mathbf{q} is the heat flux computed from the per-atom kinetic energy, potential energy and stress tensor using the following equation:

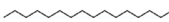

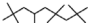

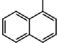
$$\mathbf{q} = \frac{1}{V} \left(\sum_{i=1}^N (ke_i + pe_i) \mathbf{v}_i - \sum_{i=1}^N \mathbf{S}_i \mathbf{v}_i \right) \quad (6)$$

where ke_i and pe_i correspond to the kinetic and potential energy of atom i , N is the total number of atoms in the system, \mathbf{v}_i is the atom velocity vector, and \mathbf{S}_i is the per-atom stress tensor.

The modelling system is constructed with 2000 biodiesel (or diesel) molecules randomly distributed in a box as shown in Fig. 1. The edge length of the box is set at a relatively large value of 20 nm to avoid atom overlapping. Energy minimization simulation is firstly performed to relax the system. Equilibrium run of 2 ns with *NPT* ensemble is followed to compress/expand the system to the target temperature and pressure. Another 1 ns

Table 2

Chemical compound names, chemical formulas, molecular structures, molecular weights and composition of diesel.

Common Name	Molecular Formula	Molecular Structure	Molecular Weight (g/mol)	Composition (mol %)
<i>n</i> -Hexadecane	<i>n</i> -HXD C ₁₆ H ₃₄		226.44	21.6
<i>n</i> -Octadecane	<i>n</i> -OTD C ₁₈ H ₃₈		254.49	15.5
2,2,4,4,6,8,8-Heptamethylnonan	HMN C ₁₆ H ₃₄		226.44	26.0
<i>trans</i> -Decalin	DCA C ₁₀ H ₁₈		138.25	16.2
1-Methyl Naphthalene	1-MNT C ₁₁ H ₁₀		142.20	20.7

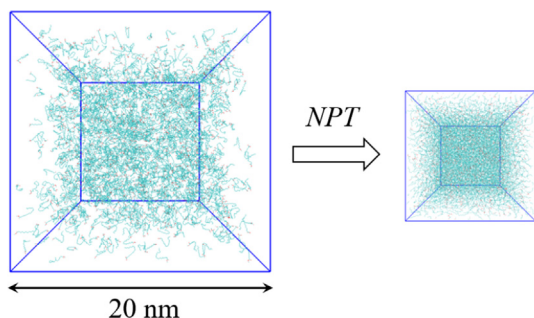


Fig. 1. Equilibration of the isotropic system in *NPT* ensemble, which can be followed by *NVT* and *NVE* ensemble for production run. The computational boxes are in perspective view.

simulation run is performed with *NVT* ensemble for further equilibrium before the production run in *NVE* ensemble.

2.2.4. Critical properties and surface tension

For the prediction of critical properties and surface tension based on the VLE modelling, fuel molecules are distributed randomly in a rectangular box of $8 \times 8 \times 32$ nm in the x, y and z directions as shown in Fig. 2 (a). After energy minimisation, an annealing simulation is performed at 1 bar with an anisotropic *NPT* ensemble in the z direction. The box is compressed in the z direction in cooling condition of 250 K for 0.5 ns and then, expanded by a linear increase of temperature up to 300 K in 1.5 ns. After that, the system is maintained for 2 ns at 300 K for further equilibrium. The liquid film generated is shown in Fig. 2 (b). Before the VLE simulation in *NVT* ensemble, the z edge of the box is scaled up by a factor of 3 based on the average length of the z edge during the last 1 ns trajectory in the *NPT* simulation. The liquid film is then placed in the centre of the elongated box as shown in Fig. 2 (c). The liquid film is heated with a rate of 0.1 K/ps from 300 K to the target temperature and then, it is maintained at the temperature for the production run for 10 ns. This methodology has been validated in previous work using hydrocarbon fuels [14].

To obtain the critical properties, the densities of liquid and vapour phases, *i.e.* ρ_L and ρ_V in VLE, are obtained by fitting the density profile to the equation expressed as:

$$\rho(z) = \frac{1}{2}(\rho_L + \rho_V) - \frac{1}{2}(\rho_L - \rho_V) \tanh\left(\frac{2(z - z_0)}{d}\right) \quad (7)$$

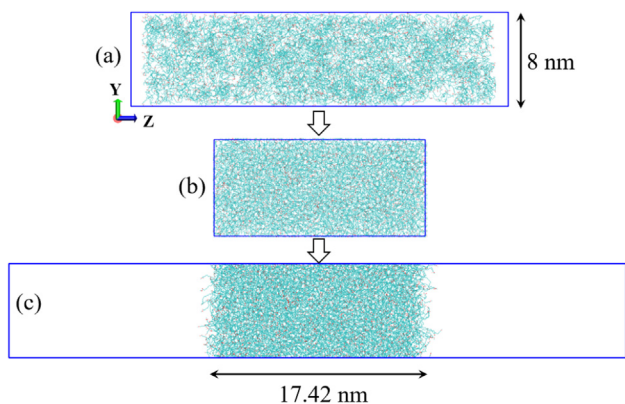


Fig. 2. (a) Snapshot of the initial biodiesel computational box; (b) after 4 ns annealing-equilibrium simulation in anisotropic *NPT* ensemble; (c) elongated box in z direction for production run. The computational boxes are in orthographic view.

where z_0 and d are the fitting parameters related to the position where the density is half between ρ_L and ρ_V , d is the width of the liquid–vapour interface.

Critical temperature (T_c) and critical density (ρ_c) are extrapolated using the density scaling law and the law of rectilinear diameters. The critical pressure (P_c) is estimated using ρ_L in the Rackett equation described by Messerly *et al.* [27]. The equations are expressed as:

$$\rho_L - \rho_V = A(T_c - T)^\beta \quad (8)$$

$$\frac{1}{2}(\rho_L + \rho_V) = \rho_c + B(T_c - T) \quad (9)$$

$$P_c = \frac{R_g T_c \rho_c}{M} \left(\frac{\rho_c}{\rho_L}\right)^{\left(1 - \frac{T}{T_c}\right)^\chi} \quad (10)$$

where A and B are fitting parameters, β is the critical exponent with a universal value of 0.325 [14,23], R_g is the gas constant, M is the molecular weight, and χ is an empirical constant equal to $2/7$ [14].

A method to compute the surface tension in MD simulations was developed by Kirkwood and Buff [28]. It computes the surface tension as an integral of the difference between the normal and tangential pressures:

$$\gamma = \frac{1}{2} \int_{-\infty}^{\infty} (P_{\perp}(z) - P_{\parallel}(z)) dz \quad (11)$$

where $P_{\perp}(z)$ is the pressure component normal to the surface and $P_{\parallel}(z)$ is the pressure component parallel to the surface. In the case of an interface between two fluid phases, the integral in Equation (11) can be replaced with an ensemble average of the difference between the normal and tangential pressures, using the equation expressed as:

$$\gamma = \frac{1}{2} L_z \left(\langle P_{zz} \rangle - \frac{1}{2} (\langle P_{yy} \rangle + \langle P_{xx} \rangle) \right) \quad (12)$$

where L_z is the length of the box in z axis, $P_{\alpha\alpha}$ is the diagonal component of the pressure tensor.

2.2.5. Mixing in bath gas

To study the gas phase transport properties, the mass diffusivity of fuels in dilute bath gases is calculated. According to previous studies of Chae *et al.* [15,16], there is no difference of mutual diffusion coefficient of alkanes in bath gas of N_2 with different concentrations of 1%, 5% and 10%. In this study, 1000 fuel molecules are put randomly in the cubic box with fuel mole concentration of 1%. EMD simulation of 12 ns is performed for each case which includes 1 ns *NVT* simulation to control the temperature, followed by 11 ns *NVE* simulation. The diffusion coefficient of fuel molecules is calculated over the last 10 ns simulation. In EMD simulation, the diffusion coefficient can be determined by the slope of the mean-squared displacement (MSD) of fuel molecules based on the Einstein equation:

$$D_i = \lim_{t \rightarrow \infty} \frac{1}{6N_i t} \left\langle \sum_{j=1}^{N_i} (\mathbf{r}_j(t) - \mathbf{r}_j(0))^2 \right\rangle \quad (13)$$

where D is the diffusion coefficient, N_i is the number of molecules of fuel i , and \mathbf{r}_j is the position of the j^{th} molecule of fuel i .

3. EMD simulation results and discussions

3.1. Density

The predicted densities of biodiesel and diesel are shown in Fig. 3. After comparison with other force fields, it was observed that the TraPPE can reproduce the density of alkanes with high accuracy (only 1% different from experiments) [29]. Density of practical fuel mixtures depends on the composition and conditions. At 0.1 MPa and 298 K, density of biodiesel is in the range of 0.870–0.895 g/ml, higher than conventional diesel, which is in the range of 0.810–0.860 g/ml [1]. In the MD simulation, densities of rapeseed biodiesel and diesel are 0.878 g/ml and 0.825 g/ml respectively, which fall in the range of experimental results. For fuels at isothermal conditions, density is fitted according to the Tait correlation [30] expressed as:

$$\frac{\rho - \rho_0}{\rho} = A \log\left(\frac{B + P}{B + P_0}\right) \quad (14)$$

where ρ_0 is the density at P_0 which is 10 MPa here, A and B are parameters which can be obtained by fitting the scattered density data points.

To avoid the possible solidification induced by high pressure [6,29], the densities of biodiesel are predicted up to 200 MPa at 300 K. In Fig. 3 (a), the predicted densities fit well with the Tait equation at isothermal conditions, and density of biodiesel is 5.39% and 5.43% higher than that of diesel at 300 K and 400 K respectively. The graph shows small variations in density for both biodiesel and diesel as the pressure increases. In Fig. 3 (b), the relative difference in density between biodiesel and diesel at isobaric condition of 5 MPa increases sharply from 6.69% at 400 K to 86.55% at 900 K, and then decreases gradually to 42.17% at 1500 K. However, at 15 MPa, the relative difference increases gradually from 6.13% at 400 K to 25.68% at 1500 K. Unlike the discontinuity of densities in liquid to gas phase transition at normal pressure, the isobaric densities at 5 MPa and 15 MPa vary gradually and change almost linearly at 15 MPa.

3.2. Viscosity

The calculation of biodiesel viscosity using the EMD-GK method at 0.1 MPa and 300 K is shown in Fig. 4. It has been confirmed that the viscosity is independent of different thermostats in ensembles of NVT and NVE, and the finite size effect of simulation system is negligible [31]. However, the simulation duration would affect the convergence of the viscosity. From the normalised ACF of the pressure tensor with sampling frequency of 1 time step shown in Fig. 4 (a), the correlation function $C(t)$ decays rapidly to zero at the initial short stage of 0.01 ps, and then fluctuates around zero

until a large fluctuation appears at the late stage of 8–10 ps. The corresponding viscosity is shown in Fig. 4 (b), where viscosities of the three different off-diagonal pressure tensors show a strong correlation until 0.4 ps as highlighted in the zoomed-in region. After reaching the plateau at around 2–4 ps, a gradual deviation between the viscosities in the late stage is observed. Although averaging the viscosities over three different pressure tensors can facilitate the convergence to some extent, the viscosity value hardly converges to a constant. The fluctuation of the integral makes it difficult to identify the plateau of viscosity from a single trajectory.

To calculate the viscosity with more accuracy (than identifying the plateau region manually), Zhang *et al.* [32] developed the time decomposed method (TDM) by fitting the averaged GK viscosity in a double stretched exponential function given by:

$$\eta(t) = A\alpha\tau_1(1 - e^{-t/\tau_1}) + A(1 - \alpha)\tau_2(1 - e^{-t/\tau_2}) \quad (15)$$

where A , α and τ_1 and τ_2 are fitting parameters.

The averaged results, fitted value and standard deviation of 20 independent trajectories are shown in Fig. 4 (c). The convergence is greatly improved after averaging over 20 independent trajectories, and the standard deviation increases with the time evolution. The final viscosity of the fitted value is 1.59 mPa·s. In general, the kinematic viscosity (μ) of biodiesel at 40 °C is of interest in standard specifications. Compared with the given reference range of 1.9–6.0 mm²/s for 12 different biodiesel [33], the corresponding predicted kinematic viscosity is 1.57 mm²/s using EMD simulation. The TraPPE force field is likely to underestimate the viscosity to some extent, mainly because the molecular model is united atoms rather than all atoms [34].

The pressure and temperature dependence of the viscosities of biodiesel and diesel from GK-TDM method is shown in Fig. 5. The pressure and temperature dependence of GK viscosity is fitted according to the equation developed by Kashiwagi *et al.* [35] and Das *et al.* [36]:

$$\ln \frac{\eta(P)}{\eta_0} = A \ln\left(\frac{B + P}{B + P_0}\right) \quad (16)$$

$$\eta(T) = \exp\left(\frac{A}{T - B}\right) - C \quad (17)$$

where η_0 is the shear viscosity at pressure $P_0 = 10$ MPa, A , B and C are fitting parameters.

Both isothermal and isobaric viscosities of biodiesel and diesel display a good fit to the curves described by Equations (16) & (17). At normal conditions, the viscosity of most biodiesel fuels is significantly higher than that of conventional diesel by a factor of 2 [33]. This also applies to high pressure conditions. At isothermal conditions of 300 K, the viscosity of biodiesel is higher than that of

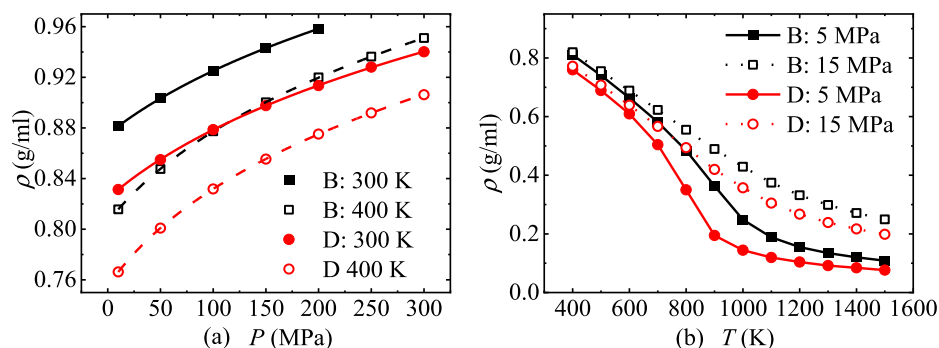


Fig. 3. Pressure and temperature dependence of densities of biodiesel (B) and diesel (D), where lines in (a) are fittings while lines in (b) are connection between the scattered data points, and pressure starts from 10 MPa in isothermal conditions.

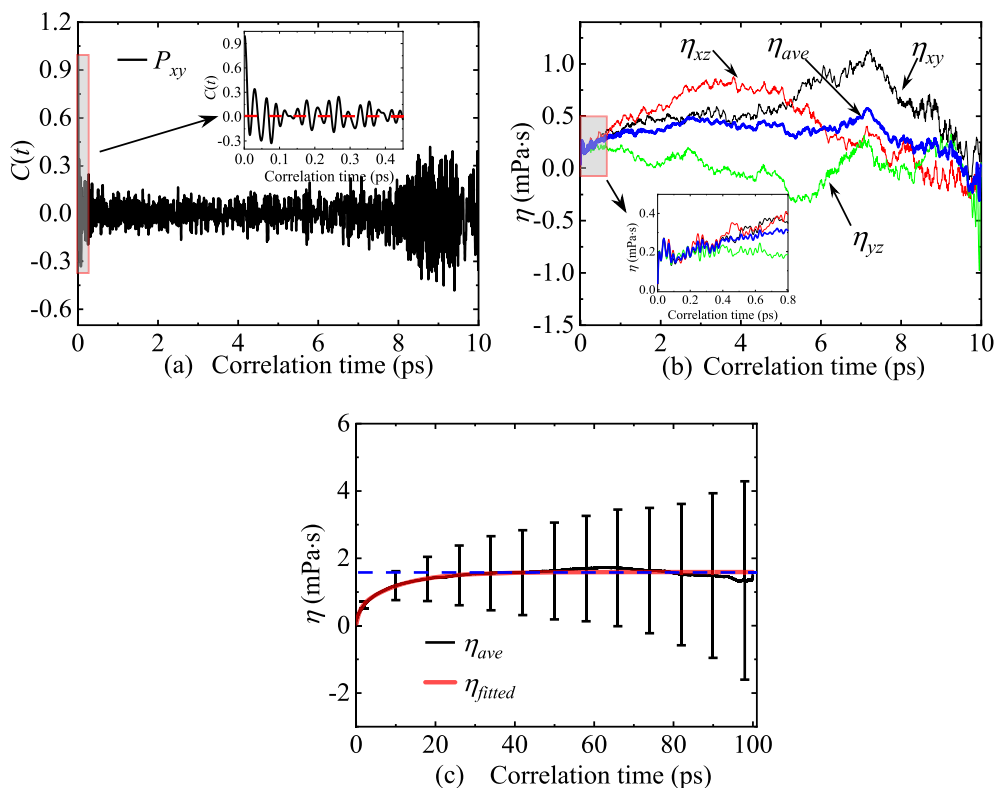


Fig. 4. (a) Normalised correlation function $C(t)$ of the pressure tensor P_{xy} at 0.1 MPa and 300 K; (b) viscosities of the three off-diagonal pressure tensors from a single trajectory and the averaged result; (c) the black line is the averaged running integral over 20 independent trajectories, while the red line is the fitted curve according to Equation (15), error bars represent the standard deviation between the trajectories.

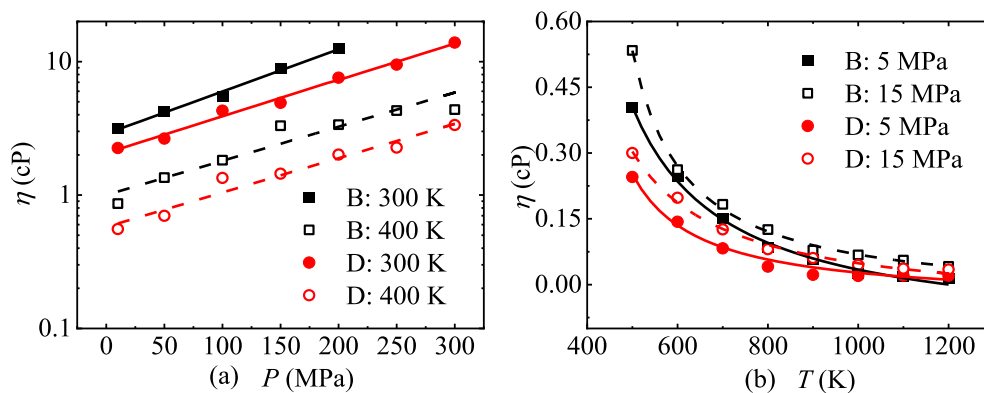


Fig. 5. Pressure and temperature dependence of viscosity of biodiesel and diesel, where lines are fitted curves according to Equation (16) and Equation (17).

diesel by a factor around 1.28–1.80, and these values increase up to 1.36–2.29 at 400 K. Biodiesel viscosities at 300 K are 2.67–3.73 times higher than those at 400 K, while diesel viscosities at 300 K are 3.19–4.19 times higher than those at 400 K. Although absolute differences between biodiesel and diesel diminished rapidly at isobaric conditions, the relative difference at 15 MPa is still between 20.43% and 52.81% for temperatures above 900 K. The difference between biodiesel and diesel on viscosity is attributed to the fuel composition and molecular structures. This has been demonstrated in the mixing rules of some empirical equations used to calculate the kinematic viscosity of biodiesel from neat FAMES at normal conditions as reviewed by Abel *et al.* [9]:

$$\ln \mu = \sum_{i=1}^n x_i \ln \mu_i \quad (18)$$

$$\mu_i = -12.503 + 2.496 \ln M_i - 0.178 N_{d,i} \quad (19)$$

where n is the number of surrogate molecules, x_i is mole fraction of component i , M is molar mass and N_d is the number of double bonds. The kinematic viscosity of biodiesel predicted using the mixing rule is 1.43 mm²/s at 313 K, which is very close to the EMD result.

From Equation (19), viscosity of neat FAMES increases with chain length, and higher unsaturation leads to lower viscosity. It is generally considered that *trans*-configuration will lead to higher viscosity than *cis*-configuration, while the location of double bond has the least effect [33]. As shown in Table 1 and Table 2, the majority of the compounds of FAMES in biodiesel have longer chain length than the n -alkanes in diesel. The viscosity of FAMES is higher than that of the corresponding n -alkane and the branched

alkane. As known from the experimental results, viscosity of methyl myristate ($C_{15}H_{30}O_2$) is 1.91 mPa·s at 333.15 K [37] which is higher than viscosity of HXD (1.84 mPa·s) and HMN (1.89 mPa·s) at 323.15 K [38,39].

3.3. Thermal conductivity

The results of thermal conductivity of biodiesel at 0.1 MPa and 400 K using the EMD-GK method are shown in Fig. 6. The normalised ACF of heat flux shows comparable decaying trend with that of the pressure tensor. It drops to zero at 11 fs and then fluctuates around zero with much smaller standard deviation compared to the ACF of the pressure tensor as shown in the highlighted region of Fig. 6 (a). Compared with the convergence of viscosity, the thermal conductivities from three different heat fluxes are closer to each other in the time of 2–6 ps in Fig. 6 (b). The smaller fluctuation in the middle stage allows to identify the plateau value effectively. The averaged value of thermal conductivity over 20 independent trajectories increases to the peak value at 78 fs, and then, it decays gradually to almost a constant value as shown in the highlighted region of Fig. 6 (c). The standard deviation stays stable after 50 ps, thus the final value of thermal conductivity is determined by the mean value in the time of 20–80 ps. The predicted thermal conductivity values of biodiesel and diesel are 0.18 W/mK and 0.26 W/mK, respectively. It should be noted that experimental thermal conductivity of multicomponent fuel mixtures is very scarcely reported, and reliable predictive models are highly needed [40].

The effects of pressure and temperature on thermal conductivity are shown in Fig. 7. Reliable fitting equations to describe the isothermal and isobaric thermal conductivities of fuel mixtures are lacking. At isothermal conditions with pressure range 10–300 MPa, the thermal conductivity of the fuel shows low depen-

dence on pressure. The difference between biodiesel and diesel at isothermal condition mainly exists at pressure below 200 MPa, where biodiesel has lower thermal conductivity than diesel. At isobaric conditions with temperature range 500–1200 K, thermal conductivity correlates linearly with the temperature. Diesel has higher thermal conductivity than biodiesel by 30.48% – 59.63% at 5 MPa and 41.68% – 50% at 15 MPa. At supercritical dense gas phase above 800 K, the fuel thermal conductivity is clearly higher at 15 MPa than at 5 MPa.

3.4. Critical property and surface tension

The snapshots of the biodiesel VLE simulation are shown in Fig. 8. The results of the MD-VLE simulation of biodiesel, *i.e.*, the density profile along the z direction, the vapour-liquid coexistence curves and the critical points are shown in Fig. 9.

As shown in Fig. 9 (a)–(b), the density of liquid core decreases with temperature, contrary to what happens to the density in gas phase. As the temperature approaches the critical temperature, the interface thickness increases, and vapour-liquid interface diminishes. For instance, the interface thickness of biodiesel increases from 1.33 nm at 450 K to 3.81 nm at 650 K, and the interface thickness of diesel increases from 1.02 nm at 400 K to 5.24 nm at 600 K. After mapping the densities of fuels when the liquid and gas phases reach equilibrium, the vapour-liquid coexistence curves are shown in Fig. 9 (c).

Critical properties of the multicomponent fuel mixtures depend on molecular structure and composition. The critical points of biodiesel and diesel surrogate fuels are listed in Table 3. The predicted critical properties of biodiesel and diesel with different MD setups are summarised in Table 4. For FAMES, T_c increases with the chain length, while P_c decreases with the chain length. Effect of unsaturation on critical properties is not as prominent as chain length.

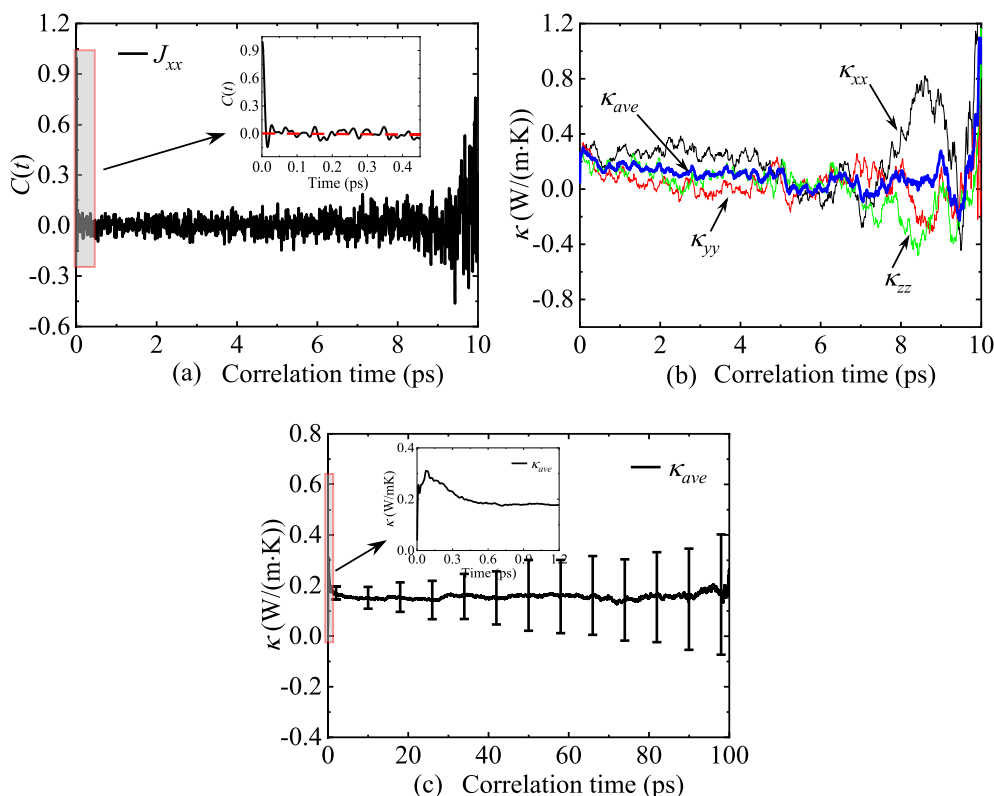


Fig. 6. (a) Normalised $C(t)$ of heat flux J_{xx} of biodiesel at 0.1 MPa and 400 K; (b) convergence of thermal conductivity from three different heat fluxes and the averaged value in a single trajectory; (c) averaged results of 20 independent replicated trajectories.

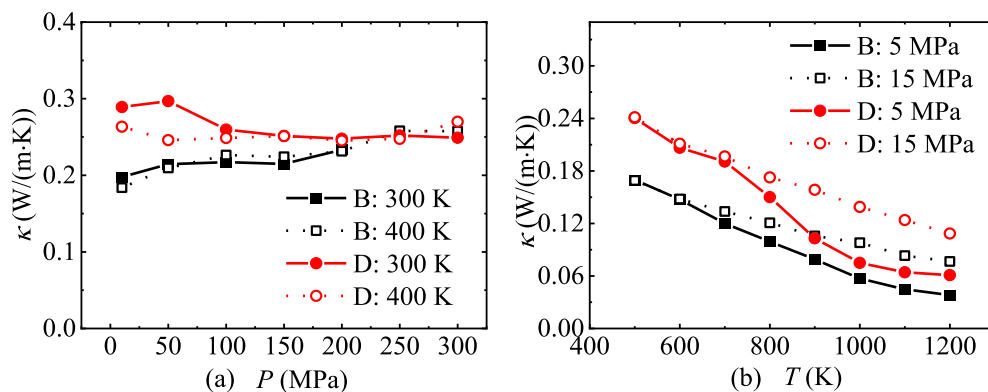


Fig. 7. Pressure and temperature dependence of thermal conductivity of biodiesel and diesel.

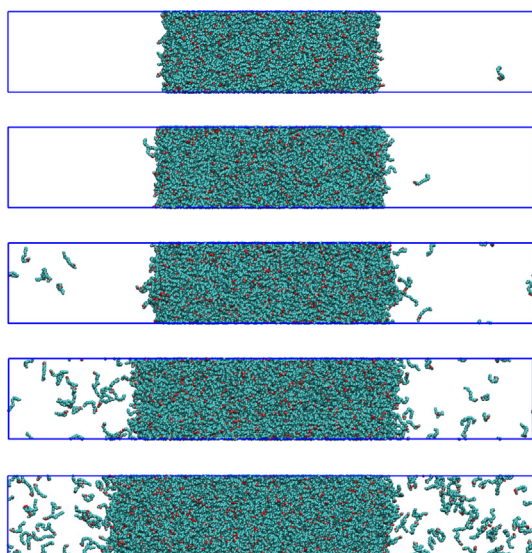


Fig. 8. Final snapshots after 10 ns VLE simulation of biodiesel; from top to bottom: 450 K, 500 K, 550 K, 600 K and 650 K respectively.

The critical temperatures and pressures of biodiesel and diesel mixtures can also be calculated based on the critical properties of the corresponding surrogate fuels listed in Table 3, together with the mixing rules developed by Li *et al.* [41]. Table 4 shows the comparison between the results from the mixing rules and the MD results.

It should be noted that the vacuum space shown in Fig. 8 on both sides of the liquid films during the VLE simulation makes the system inhomogeneous. Under this circumstance, ignoring long-range dispersion force of the LJ potential can result in inaccurate prediction of the critical properties and significant underestimation (which can be as high as 50%) of the surface tension [44]. Similar to the Coulomb force, one can adopt the PPPM solver to compensate the truncation of dispersion forces in reciprocal-space *i.e.*, dispersion-PPPM. The predicted results after considering the long-range LJ interaction are listed in Table 4.

From the results in Table 4, it can be seen that biodiesel has higher critical temperature and lower critical pressure in all methods. For critical temperature, although overestimated slightly, MD with dispersion-PPPM can reproduce critical temperature better than the truncated LJ interaction. The critical pressures of biodiesel and diesel from the MD-VLE are about 1.7–2.2 times higher than the results from the mixing rules. Compared with the accurate reproduction of the critical properties of pure hydrocarbons [14],

the MD-VLE method with TraPPE-UA force field can quantitatively predict the critical temperature of fuel mixtures, but only qualitatively for the critical pressure. Further investigation on the capability of MD-VLE method on predicting critical pressure of practical fuel mixtures is needed.

Time evolution of biodiesel surface tension during the VLE simulation is demonstrated in Fig. 10 (a). The final surface tension is the time averaged value over the 10 ns simulation. The predicted surface tensions of biodiesel and diesel at different temperatures are shown in Fig. 10 (b), which are fitted linearly with temperatures. The surface tension of FAMEs increases with the chain length and the degree of unsaturation as that reflected in the empirical equation developed by Phankosol *et al.* [2] in order to estimate surface tension of biodiesel mixtures at temperatures between 30 and 80 °C according to the FAME composition, *i.e.*, $\gamma = 60.211 - 0.4307N_C - 0.1125T + 0.00207N_C T + 3.676N_d - 0.00893N_d T$, where N_C and N_d are average numbers of carbon atoms and double bonds of biodiesel mixtures.

The surface tension obtained from the MD-VLE simulation with LJ cut off at distance of 1.4 nm can be 16.01%–61.77% lower than the results taking consideration of the long-range dispersion. Surface tension of biodiesel estimated from the dispersion-PPPM approximates the results obtained from the empirical equation by Phankosol *et al.* [2]. The surface tension of biodiesel is significantly higher than conventional diesel and hence poor atomization might occur when the fuel is injected into the combustion chamber. The disappearance of the surface tension above critical temperatures indicates the shifting from the conventional two-phase droplet evaporation to diffusion dominated mixing process in supercritical conditions.

3.5. Fuel mixing with N_2

The typical condition to study supercritical combustion is 6 MPa and 900 K which is above the critical points of biodiesel, diesel and N_2 ($T_c = 126.19$ K, $P_c = 3.40$ MPa). There is a lack of investigation on the diffusion coefficient of practical fuel molecules in N_2 in supercritical conditions. In this study, when simulating the mixing process, fuel aggregation is observed for biodiesel in N_2 at the lower temperature of 400 K as shown in the snapshots in Fig. 11. The cluster recognition is performed using OVITO [26], and the intermolecular cut-off distance to discriminate the clusters is set to be 4 Å [45]. The time evolution of biodiesel and diesel aggregation regarding the aggregation cluster numbers (N_c) and the size of the largest aggregation cluster (S_c) at temperatures of 400 K and 500 K is shown in Fig. 12. At temperature above 600 K, no aggregation phenomenon occurs for biodiesel or diesel at 5 MPa and 15 MPa. To study the mobility of fuel molecules in bath gas, diffusion coef-

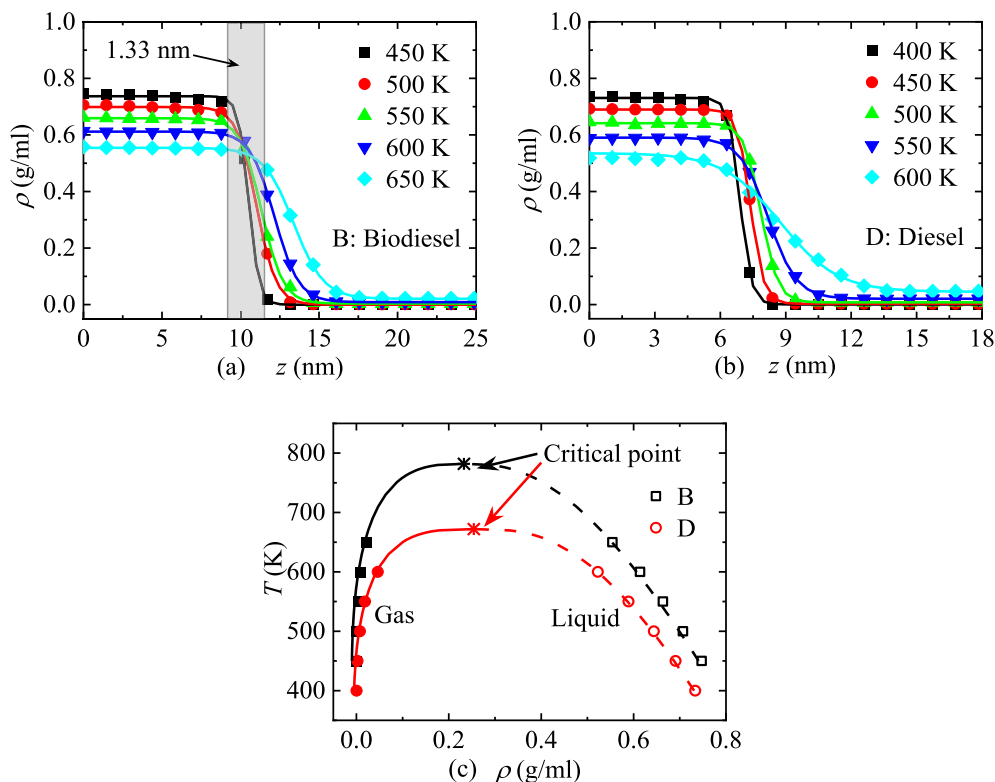


Fig. 9. (a)-(b) Density profiles of biodiesel and diesel respectively, shown as a function of the distance from the centre of liquid film, where lines are fitted curves according to Equation (7), and the shaded area in (a) indicates the vapour-liquid interface at 450 K; (c) vapour-liquid coexistence curves of biodiesel and diesel, where lines are fitted curves, the fitting parameters A and B in Equations (8)-(9) for biodiesel are 0.0895 and 0.0004, for diesel are 0.1197 and 0.0004 respectively.

Table 3

The critical properties of biodiesel surrogate fuels, taken from the work Evangelista *et al.* [42], and the values of diesel surrogate fuels taken from the work of Lin *et al.* [43].

Surrogate fuels	MP	MS	MO	ML	MLN	<i>n</i> -HXD	<i>n</i> -OTD	HMN	DCA	1-MNT
T_c (K)	769	790	792	793	794	723	747	693	687	772
P_c (MPa)	1.38	1.26	1.28	1.31	1.33	1.40	1.29	1.57	3.20	3.60

Table 4

Comparison between the MD-VLE method and empirical equation on the prediction of critical properties of biodiesel and diesel.

	T_c (K)		P_c (MPa)	
	Results from mixing rules	MD	Results from mixing rules	MD
Biodiesel	792	782* 800#	1.32	2.50* 2.93#
Diesel	722	672* 739#	2.15	3.90* 3.76#

*: LJ cut off at distance of 1.4 nm, #: dispersion-PPPM accounts for long-range LJ interaction.

ficients of each fuel surrogate in N_2 are calculated at 600 K and above, as shown in Fig. 13 for some of the representative fuel surrogates.

To quantitatively describe the aggregation process of different systems, the reduced values are used in Fig. 12, i.e., N_c is defined as the ratio of the number of clusters over the overall number of fuel molecules, and S_c is the ratio between the number of fuel atoms in the largest cluster over the overall number of fuel atoms. Fuels with higher boiling temperature tend to possess lower volatility. Boiling temperature values of different fuel surrogate molecules vary in a way that: FAME > *n*-alkanes > branched alkane, and fuel molecules with longer chain or higher molecular weight always have higher boiling temperature [6]. As listed in Table 1

and Table 2, biodiesel mainly consists of FAMES with chain length of C_{18} accounting for 95.7%, while the molecule having the longest chain in diesel is *n*-alkane of C_{18} which only accounts for 15.5%. The boiling temperature of some practical biodiesel ranges from 573 K to 623 K, while boiling temperature of diesel can be as low as 453 K [46,47]. It can be seen in Fig. 11 that, in general, biodiesel is more likely to aggregate and generate clusters than diesel.

Temperature and pressure affect the cluster growth rate and the cluster size distribution during condensation. The lower ambient temperature and higher pressure can promote the aggregation, but the effects are different when it comes to different fuels [48]. The aggregation of diesel is not prominent or even not existent at 15 MPa and 400 K after long simulation time until a slow

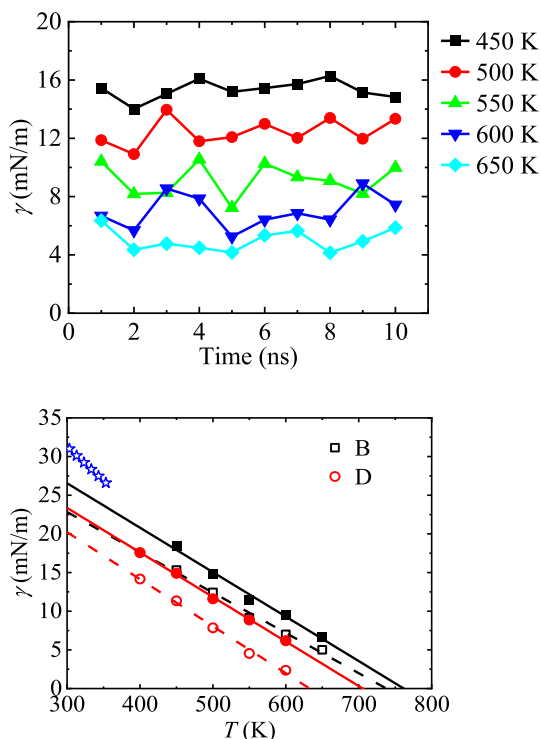


Fig. 10. (a) Time evolution of the surface tension of biodiesel during the VLE simulation; (b) surface tension of biodiesel and diesel as a function of temperature, where hollow symbols are results of Lj cut off at distance of 1.4 nm, solid symbols are results considering long-range Lj interaction, the solid and dashed lines are fitted lines, and blue stars indicate the biodiesel surface tension estimated using the empirical equation by Phankosol et al. [2].

increase of the largest cluster occurs after 8.50 ns. There is a significant difference in the clustering regularity of biodiesel at 400 K and 500 K under 15 MPa. For biodiesel at 400 K, the initial condensation rate is higher, and the formation of the critical nuclei and the merge of nuclei occur earlier. Therefore, the curve of S_c shows a multiple step growth and the number of clusters in the box decreases quickly. While at 500 K, biodiesel cluster size increases gradually by surface growth until the merge occurs at a later time of 11.54 ns, and the number of clusters decreases slowly.

Fig. 13 shows the diffusion coefficient results calculated from the slope of the mean-squared displacement, as that given in Equation (13). The MSD of the centre of mass of FAME molecules in N_2 shows evident fluctuations as shown in Fig. 13 (a), which is different with the perfectly smooth lines for MSD of pure alkanes in the bulk liquid state [6]. The diffusion coefficient is the linear fitting of the MSD, and the region for the linear fitting should be carefully selected to avoid the anomalous diffusion in the initial stage. Taking the example of MP at 5 MPa and 900 K shown in Fig. 13 (b), where the two-point slope of MSD is used to obtain the diffusion coefficient, it can be found that too short time intervals would result in the difficulty of convergence and noise in the diffusion coefficient. The diffusion coefficient keeps increasing until it reaches the plateau at 2–4 ns. The time evolution of the diffusion coefficient has much better convergence than 1 fs when fitting the MSD with time interval of 1 ps or longer. In this study, the diffusion coefficient is the linear fitting of MSD between 5 and 10 ns in all conditions. The effect of temperature and pressure on diffusion coefficient of MP is shown in Fig. 13 (c). The fitted constant n of 5 MPa and 15 MPa is equal to 1.93 and 1.55 respectively, and the diffusion coefficients at 5 MPa are about 2.59–3.61 times higher than those at 15 MPa.

Among different fuel surrogates, branched alkanes and cycloalkanes have higher slope of MSD than FAMES and long-chain alkanes as shown in Fig. 13 (a). The comparison of diffusion coefficients for different conditions between typical fuel surrogates with MP is shown in Fig. 13 (d), where it can be observed that the diffusivity has a direct correlation with the molecular configuration. To be specific, diffusion coefficients of DCA, 1-MNT and HMN are 1.98, 1.94 and 1.39 times larger than those of MP in the current conditions, while HXD is only 1.13 times larger than MP. If classified by molecular shape, DCA and 1-MNT are disc-like, while HMN is sphere like, and n -alkanes and FAMES are stick-like [49]. As for comparison between other FAMES with MP, the values range from 0.93 of MS to 1.00 of MO, which means the unsaturation has a negligible effect compared to molecular shape.

4. Feasibility of NEMD simulations on building large-scale database

The results presented in the previous section are based on equilibrium molecular dynamics simulations. By using EMD simulation, various thermophysical properties of fuel mixtures can be obtained by running the system into desired temperature and pressure conditions in NPT ensemble. After validating the methodology and the simulation setups in normal conditions, the MD simulation systems and the parameters can be extended to other conditions. It was demonstrated that the EMD-GK method used in this study would have universality and it is independent of the simulation conditions. This indicates that it is feasible to use EMD to build large-scale databases of fuel properties, considering that high performance computing resources are becoming more available and affordable. This study demonstrated that EMD is a reliable methodology to predict the properties of practical fuel mixtures over a wide range of conditions including extreme conditions.

Besides the EMD method, nonequilibrium MD simulation provides another option to calculate thermophysical properties. Although NEMD offers a way to simulate systems which do not adhere to the conventional equilibrium model and it may provide a better physical description of the systems for certain conditions, the universality of the setup parameters remains an open question. In this study, the feasibility of NEMD in building large-scale databases of fuel properties was also explored. Here, the NEMD method on thermal conductivity prediction is used as an example to investigate the feasibility of this method to obtain transport properties. To calculate the thermal conductivity κ in the NEMD simulation according to Fourier's law, i.e., $\mathbf{q} = -\kappa \nabla T$ one can impose temperature gradient in a simulation box and then measure the resulting heat flux. Alternatively, the reverse NEMD approach by Müller-Plathe [50] can be used, in which the heat flux is created in a system by exchanging the kinetic energy between atoms located in different regions of a simulation box as shown in Fig. 14 (a). The first slab is set to be the cold layer, while the central 11th slab is set to be the hot layer. By exchanging the velocity of the hottest atom in the cold slab with that of the coldest atom in the hot slab, an artificial energy transfer from the cold slab to the hot slab is imposed. After reaching steady state, the heat flux from the hot side to the cold side is balanced by the total kinetic energy transferred by the swaps. The thermal conductivity is the ratio of the heat flux to the slope of the temperature profile, which can be obtained as:

$$\kappa = \frac{\sum_{\text{trans}} ke}{2L_x L_y \Delta t} \left(\frac{dT}{dz} \right)^{-1} \quad (20)$$

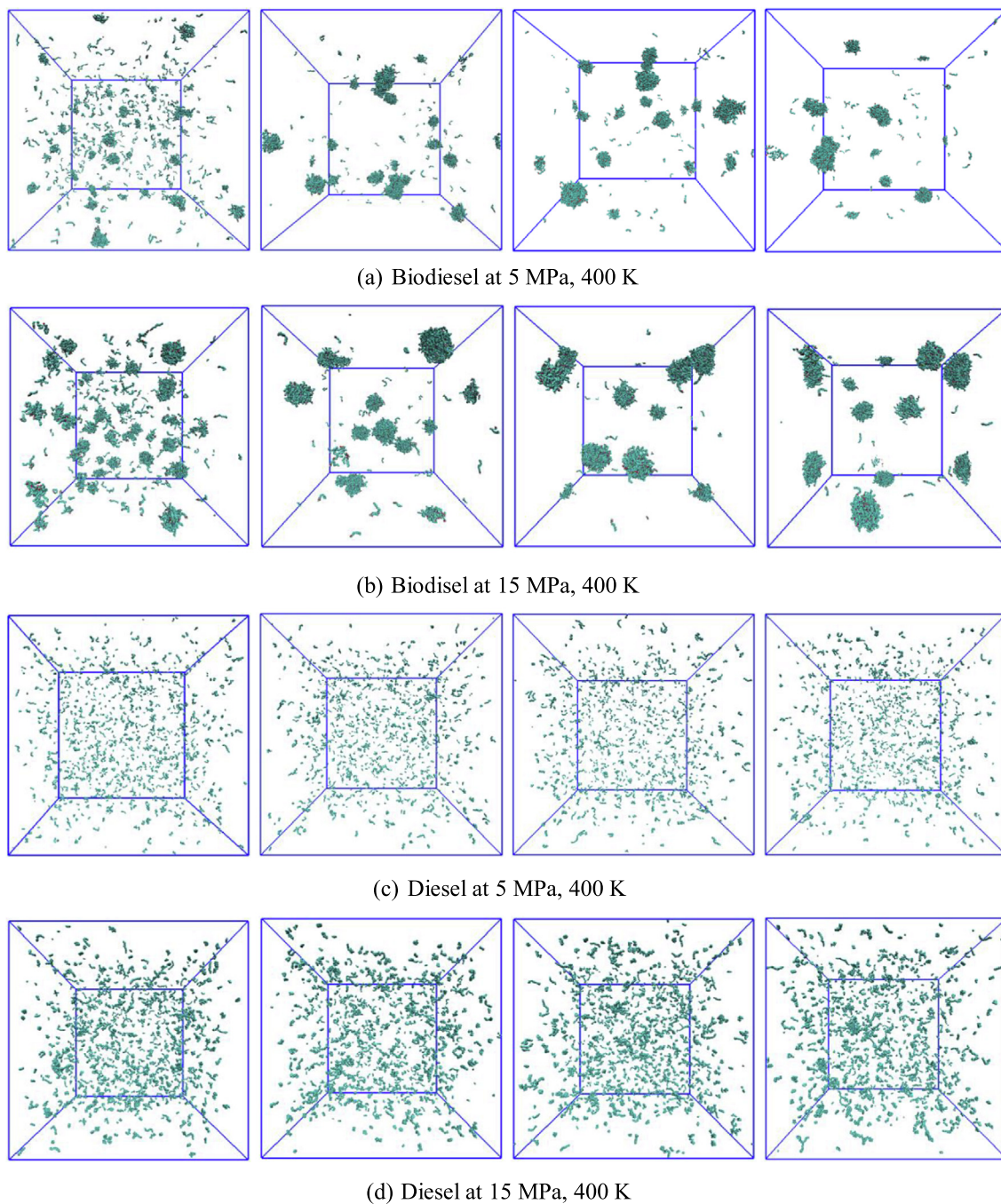


Fig. 11. Time evolution of the snapshots to indicates the effect of temperature and pressure on fuel aggregation, from left to right: 1 ns, 5 ns, 8 ns and 10 ns; N_2 molecules are hidden.

where the heat flux is equal to the transferred total energy divided by the time and cross-sectional area of the simulation box, and the temperature gradient is determined by the temperature T of each bin, which is given by:

$$T = \frac{1}{3N_b k_B} \left\langle \sum_{i=1}^{N_b} m_i v_i^2 \right\rangle \quad (21)$$

where N_b is the number of atoms in each slab.

A case of biodiesel at 313.15 K and 0.1 MPa conditions with different swap rates is considered, and the results are shown in Fig. 14 (b)-(c). The temperature gradient and amount of the heat flux are determined by the swap rate (inverse value of the time interval

between exchanging). All swap rates from 2.5 ps^{-1} to 20 ps^{-1} produce temperature profiles with good linearity, and the magnitude of the temperature gradient increases with the increase of the swap rate. The temperature difference between the hot and cold slabs converges after 300 ps, which means the system reaches its steady state and the generated temperature gradient is stable. However, the concomitant density gradient as a function of the position along the heat flux direction would result in inhomogeneity of the system. Also, the temperature in the cold slab can be as low as 181.46 K at swap rate of 20 ps^{-1} , which is below the melting point of FAMES and can result in anisotropy of conduction. Both the density inhomogeneity and the possible phase transition represent potential risks to the prediction, leading to deviation or even inval-

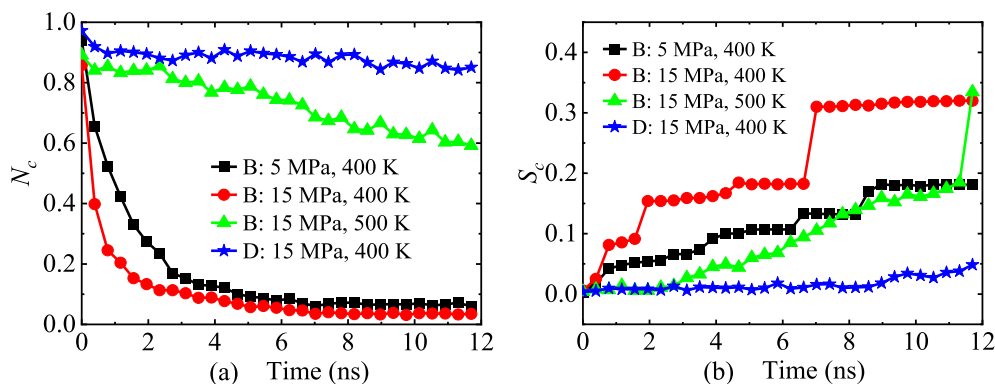


Fig. 12. (a) Time evolution of the reduced number of clusters for different systems; (b) time evolution of the size of the largest cluster in different systems.

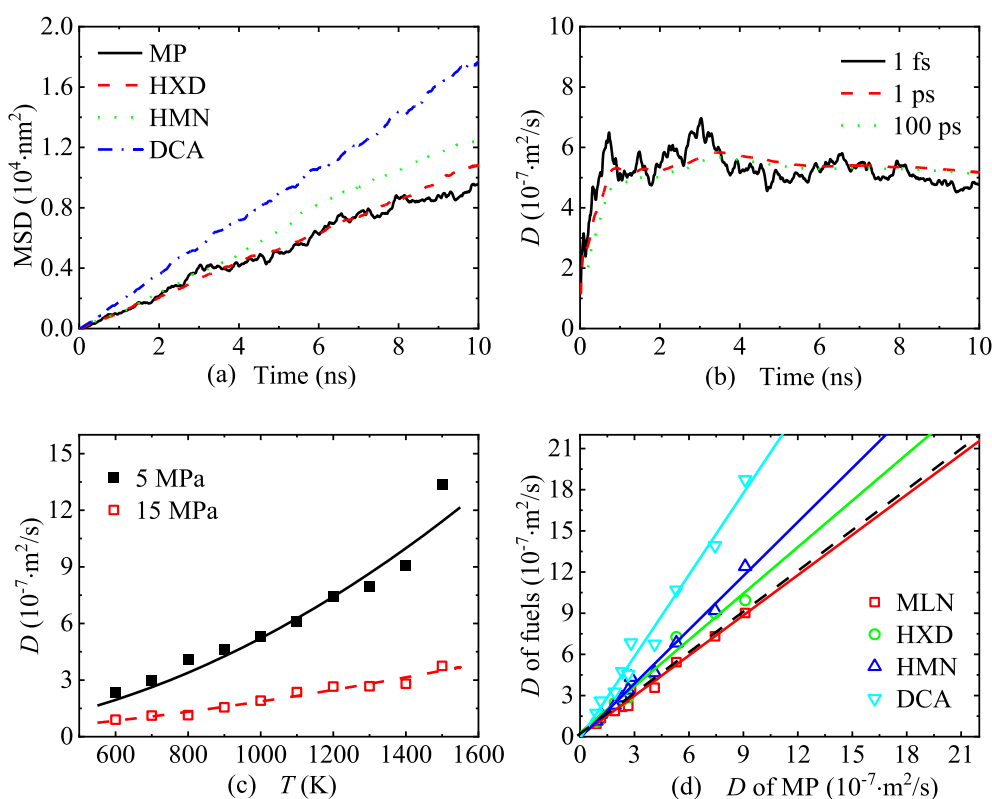


Fig. 13. (a) Representative mean-squared displacement (MSD) of fuel surrogate molecules in N_2 at 5 MPa and 900 K; (b) convergence of the diffusion coefficient of MP; (c) temperature and pressure dependence of the diffusion coefficients of MP, where lines are fitted curves according to $D = AT^n$ [15,16]; (d) comparison of diffusion coefficient between MP and different fuel surrogates, where solid lines are linear fittings, and dashed black line is for reference with the slope of 1.

identifying the results. For liquid fuels, determining the proper swap rate is a challenge, because of the conflicts between the better prediction accuracy benefited from the higher temperature gradient and the consequent deviation resulted from the higher density gradient.

The effects of swap rate on temperature and density gradients of biodiesel at extreme conditions are shown in Fig. 15. At HP compressed liquid condition with swap rates of 2.5, 5 and 10 ps^{-1} in Fig. 15 (a) and (b), the results show good linearity and negligible density inhomogeneity. The temperature of biodiesel at the cold slab with the swap rate of 2.5, 5 and 10 ps^{-1} are 284.61 K, 266.73 K and 243.72 K respectively. Considering the increased tendency of solidification of biodiesel at

HP nozzle conditions of 200 MPa [4], the swap rate should be set lower than 2.5 to avoid the possible phase transition. Although there is no phase transition for biodiesel at dense gas state of supercritical condition in Fig. 15 (c) and (d), the effects of swap rate on density gradient is evident. For example, the density at the cold slab is 3.35 times higher than that at the hot slab when the swap rate is 1 ps^{-1} , while the density gradient is insignificant at swap rate of 0.25 ps^{-1} . Therefore, the proper swap rates can vary dramatically with the conditions, and the setup parameters in normal conditions cannot be used at extreme conditions. This indicates that NEMD is not favourable for efficiently building the large-scale fuel property databases over the wide range of conditions.

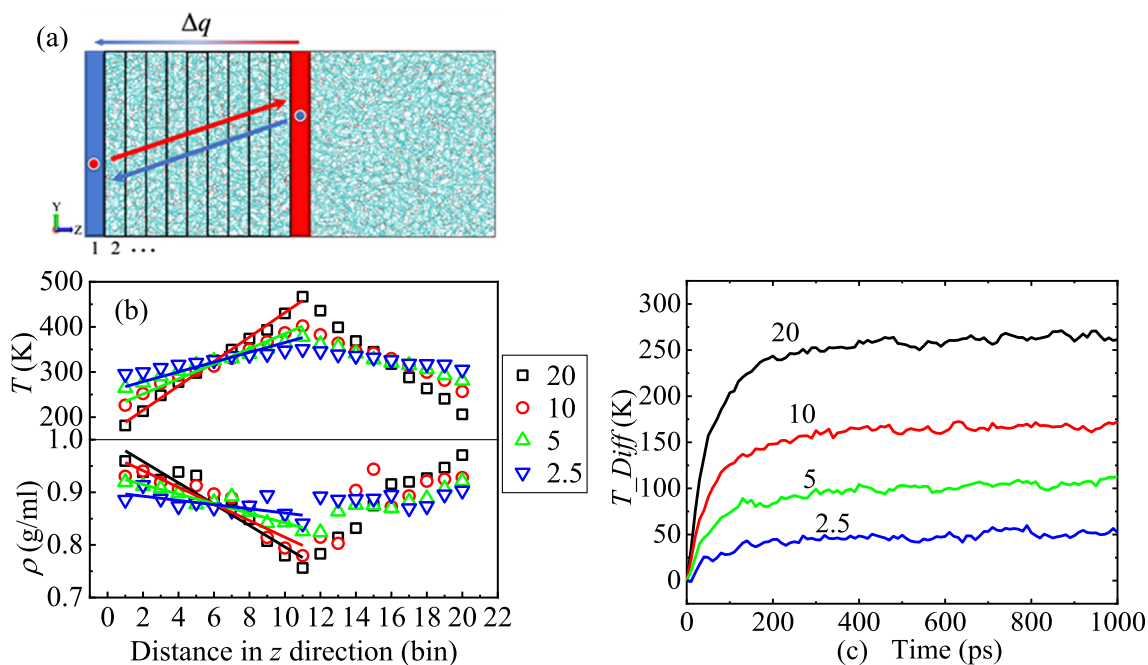


Fig. 14. (a) A schematic representation of the exchange of the kinetic energy between the atoms in the hot (red) slab and the cold (blue) slab of a simulation box in the NEMD simulation, where the simulation box is divided into 20 bins in the z direction; (b) temperature and density profiles along the z direction in the NEMD simulation with different swap rates, where lines are linear fittings; (c) convergence of the temperature difference between the hot and cold sides with different swap rates.

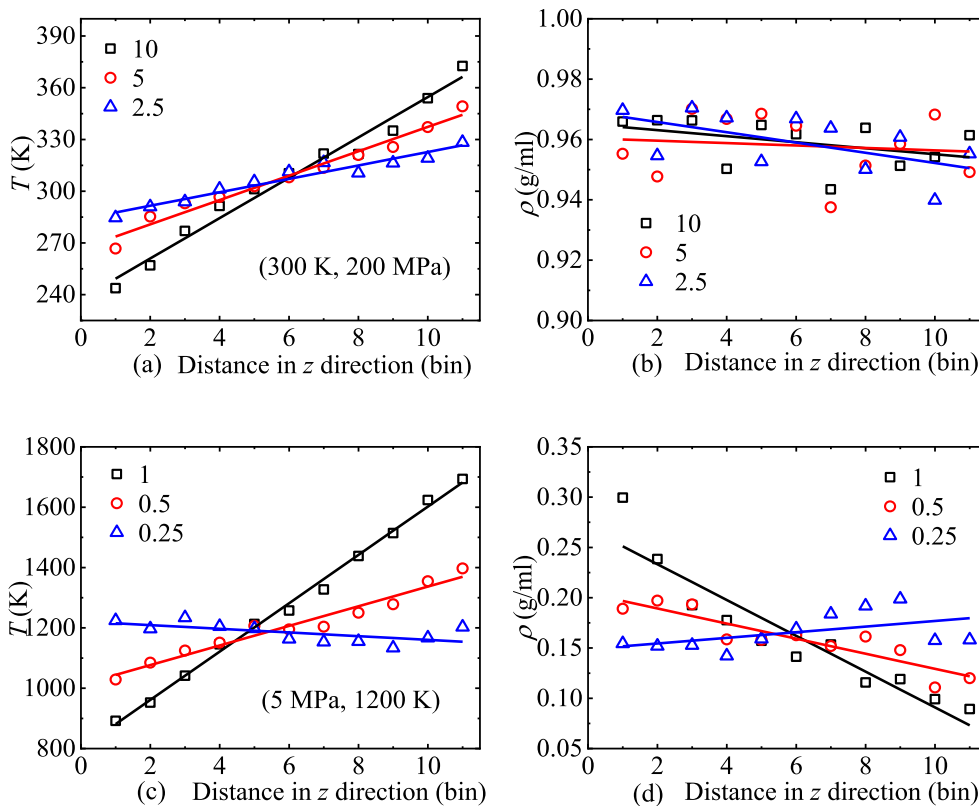


Fig. 15. Temperature and density profile of biodiesel with different swap rates at extreme conditions, (a) - (b): 300 K, 200 MPa, (c) - (d): 5 MPa, 1200 K.

5. Conclusion

In this study, molecular dynamics simulations are employed to investigate the thermophysical properties of biodiesel over a wide

range of conditions with temperatures ranging from 300 K to 1500 K, and pressures ranging from 0.1 MPa to 300 MPa. The methodology and simulation setups are examined in detail for accurate prediction of fuel properties. The properties of biodiesel are

compared with conventional diesel to guide the development and utilisation of biofuels. The main conclusions are summarised as follows.

Equilibrium molecular dynamics can obtain comparable results with experimental or empirical relations at normal conditions, and MD simulations should be carefully set up at extreme conditions. A sufficiently large number of independent trajectories is needed for viscosity and thermal conductivity calculations due to the continuous increase of deviation of the running integration in the Green-Kubo method. The long-range dispersion force should be taken into consideration when calculating the critical properties and surface tension using vapour-liquid equilibrium simulation. For calculating diffusion coefficients, the time region in the late stage should be used for linear fitting of the mean square displacement to avoid the possible anomalous diffusion. The capability of nonequilibrium MD simulations on property prediction is also investigated at normal and extreme conditions. The setup parameter in nonequilibrium molecular simulation varies with the conditions. Equilibrium molecular dynamics is therefore the better choice when building large-scale databases of fuel properties over a wide range of conditions.

Compared with conventional fossil diesel, biodiesel has higher density and viscosity at both isothermal and isobaric conditions, while the thermal conductivity varies with the conditions. Biodiesel also has higher critical temperature, higher surface tension and lower critical pressure. The increased aggregation tendency of biodiesel in bath gas is observed at temperatures of 400 K and 500 K. These results indicate that thermophysical properties of biodiesel are not as favourable as diesel in fuel injection, atomisation, spray formation and droplet evaporation.

The fuel composition and molecular structures determine the different thermophysical properties of biodiesel. The chain length of the majority biodiesel surrogates is longer than that of *n*-alkanes in diesel surrogate fuels. The branched alkanes, cycloalkanes and aromatics contribute to the favourable thermophysical properties of conventional diesel such as lower viscosity, lower surface tension and higher mobility in bath gas. In fuel utilisation applications, blending biodiesel with diesel can be a feasible way to obtain optimum physicochemical properties.

CRedit authorship contribution statement

Cheng Chen: Investigation, Methodology, Software, Writing – original draft. **Daniel Mira:** Conceptualization, Writing – review & editing. **Zhihao Xing:** Investigation, Software. **Xi Jiang:** Conceptualization, Supervision, Writing – review & editing.

Data availability

Data will be made available on request.

Declaration of Competing Interest

The authors declare that they have no known competing financial interests or personal relationships that could have appeared to influence the work reported in this paper.

References

- [1] M. Lapuerta, O. Armas, J. Rodriguez Fernandez, Effect of biodiesel fuels on diesel engine emissions, *Progr. Energy Combust. Sci.* 34 (2008) 198–223.
- [2] S. Phankosol, K. Sudprasert, S. Lilitchan, K. Aryasuk, K. Krisnangkura, Estimation of surface tension of fatty acid methyl ester and biodiesel at different temperatures, *Fuel* 126 (2014) 162–168.
- [3] L.R. Lynd, C.H. de Brito Cruz, Make way for ethanol, *Science* 330 (2010) 1176–1176.

- [4] R. Tarakowski, A. Malanowski, A.J. Rostocki, M. Kowalczyk, P. Modzelewski, et al., Could RME biodiesel be potentially harmful to modern engine? solidification process in RME, *Fuel* 146 (2015) 28–32.
- [5] R.R. Mallepally, B.A. Bamgbade, A.J. Rowane, H.B. Rokni, M.S. Newkirk, et al., Fluid properties at high pressures and temperatures: Experimental and modelling challenges, *J. Supercrit. Fluids* 134 (2018) 33–40.
- [6] C. Chen, D. Mira, X. Jiang, A molecular simulation study on transport properties of FAMES in high-pressure conditions, *Fuel* 316 (2022) 123356.
- [7] S. Xue, K. Hou, Z. Zhang, H. Liu, C. Zhu, et al., General models for prediction densities and viscosities of saturated and unsaturated fatty acid esters, *J. Mol. Liq.* 341 (2021) 117374.
- [8] G. Zhao, Z. Yuan, X. Liu, P. Wang, J. Yin, et al., Experimental investigation and molecular dynamic simulation of thermophysical properties of biodiesel surrogates: The binary mixtures of *n*-hexadecane with ethyl hexanoate and ethyl heptanoate, *J. Mol. Liq.* 317 (2020) 113980.
- [9] A.G. Ferreira, N.M.C. Talvera-Prieto, A.A. Portugal, R.J. Moreira, Models for predicting viscosities of biodiesel fuels over extended ranges of temperature and pressure, *Fuel* 119544 (2020).
- [10] C. Caleman, P.J. van Maaren, M. Hong, J.S. Hub, L.T. Costa, et al., Force field benchmark of organic liquids: density, enthalpy of vaporization, heat capacities, surface tension, isothermal compressibility, volumetric expansion coefficient, and dielectric constant, *J. Chem. Theory Comput.* 8 (2012) 61–74.
- [11] X. Nie, Z. Du, L. Zhao, S. Deng, Y. Zhang, Molecular dynamics study on transport properties of supercritical working fluids: Literature review and case study, *Appl. Energy* 250 (2019) 63–80.
- [12] X. Yang, J. Tao, Q. Liu, X. Zhang, B. Cao, Molecular dynamics simulation of thermophysical properties of binary RP-3 surrogate fuel mixtures containing trimethylbenzene, *n*-decane, and *n*-dodecane, *J. Mol. Liq.* 119258 (2022).
- [13] X. Yang, M. Zhang, Y. Gao, J. Cui, B. Cao, Molecular dynamics study on viscosities of sub/supercritical *n*-decane, *n*-undecane and *n*-dodecane, *J. Mol. Liq.* 335 (2021) 116180.
- [14] B.H. Morrow, J.A. Harrison, Vapor-liquid equilibrium simulations of hydrocarbons using molecular dynamics with long-range Lennard-Jones interactions, *Energy Fuels* 33 (2019) 848–858.
- [15] K. Chae, P. Elvati, A. Violi, Effect of molecular configuration on binary diffusion coefficients of linear alkanes, *J. Phys. Chem. B* 115 (2011) 500–506.
- [16] K. Chae, A. Violi, Mutual diffusion coefficients of heptane isomers in nitrogen: A molecular dynamics study, *J. Chem. Phys.* 134 (2011) 044537.
- [17] I.P. de Oliveira, A.R.L. Caires, K. Baskar, S. Ponnusamy, P. Lakshmanan, et al., Biodiesel as an additive for diesel-ethanol (diesohol) blend: physical-chemical parameters and origin of the fuels' miscibility, *Fuel* 263 (2020) 116753.
- [18] Y. Gong, G. Xiao, X. Ma, K.H. Luo, S. Shuai, et al., Phase transitions of multi-component fuel droplets under sub-and supercritical conditions, *Fuel* 287 (2021) 119516.
- [19] Y. Gong, K.H. Luo, X. Ma, S. Shuai, H. Xu, Atomic-level insights into transition mechanism of dominant mixing modes of multi-component fuel droplets: From evaporation to diffusion, *Fuel* 304 (2021) 121464.
- [20] O. Herbinet, W.J. Pitz, C.K. Westbrook, Detailed chemical kinetic oxidation mechanism for a biodiesel surrogate, *Combust. Flame* 154 (2008) 507–528.
- [21] Y. Qian, L. Yu, Z. Li, Y. Zhang, L. Xu, et al., A new methodology for diesel surrogate fuel formulation: Bridging fuel fundamental properties and real engine combustion characteristics, *Energy* 148 (2018) 424–447.
- [22] M.G. Martin, J.I. Siepmann, Transferable potentials for phase equilibria. 1. United-atom description of *n*-alkanes, *J. Phys. Chem. B* 102 (1998) 2569–2577.
- [23] G. Kamath, J. Robinson, J.J. Potoff, Application of TraPPE-UA force field for determination of vapor-liquid equilibria of carboxylate esters, *Fluid Phase Equilib.* 240 (2006) 46–55.
- [24] V.K. Michalis, O.A. Moulton, I.N. Tsimpanogiannis, I.G. Economou, Molecular dynamics simulations of the diffusion coefficients of light *n*-alkanes in water over a wide range of temperature and pressure, *Fluid Phase Equilib.* 407 (2016) 236–242.
- [25] S. Plimpton, Fast Parallel Algorithms for Short-Range Molecular Dynamics, *J. Comput. Phys.* 117 (1995) 1–19.
- [26] A. Stukowski, Visualization and analysis of atomistic simulation data with OVITO-the Open Visualization Tool, *Modell. Simul. Mater. Sci. Eng.* 18 (2009) 015012.
- [27] R.A. Messerly, T.A. Knotts IV, R.L. Rowley, W.V. Wilding, An improved approach for predicting the critical constants of large molecules with Gibbs Ensemble Monte Carlo simulation, *Fluid Phase Equilib.* 425 (2016) 432–442.
- [28] J.G. Kirkwood, F.P. Buff, The statistical mechanical theory of surface tension, *J. Chem. Phys.* 17 (1949) 338–343.
- [29] K.D. Papavasileiou, L.D. Peristeras, A. Bick, I.G. Economou, Molecular dynamics simulation of pure *n*-alkanes and their mixtures at elevated temperatures using atomistic and coarse-grained force fields, *J. Phys. Chem. B* 123 (2019) 6229–6243.
- [30] J. Dymond, R. Malhotra, The Tait equation: 100 years on, *Int. J. Thermophys.* 9 (1988) 941–951.
- [31] E.J. Maginn, R.A. Messerly, D.J. Carlson, D.R. Roe, J.R. Elliot, Best practices for computing transport properties 1. Self-diffusivity and viscosity from equilibrium molecular dynamics [article v1. 0], *Living J. Comput. Mol. Sci.* 1 (2019) 6324–6324.
- [32] Y. Zhang, A. Otani, E.J. Maginn, Reliable viscosity calculation from equilibrium molecular dynamics simulations: A time decomposition method, *J. Chem. Theory Comput.* 11 (2015) 3537–3546.

- [33] S.K. Hoekman, A. Broch, C. Robbins, E. Cenicerros, M. Natarajan, Review of biodiesel composition, properties, and specifications, *Renew. Sustain. Energy Rev.* 16 (2012) 143–169.
- [34] G.C. da Silva, G.M. Silva, F.W. Tavares, F.P. Fleming, B.A. Horta, Are all-atom any better than united-atom force fields for the description of liquid properties of alkanes? 2. A systematic study considering different chain lengths, *J. Mol. Liquids* 354 (2022) 118829.
- [35] H. Kashiwagi, T. Makita, Viscosity of twelve hydrocarbon liquids in the temperature range 298–348 K at pressures up to 110 MPa, *Int. J. Thermophys.* 3 (1982) 289–305.
- [36] M. Das, M. Sarkar, A. Datta, A.K. Santra, Study on viscosity and surface tension properties of biodiesel-diesel blends and their effects on spray parameters for CI engines, *Fuel* 220 (2018) 769–779.
- [37] M. Habrioux, J.-P. Bazile, G. Galliero, J.L. Daridon, Viscosities of fatty acid methyl and ethyl esters under high pressure: methyl myristate and ethyl myristate, *J. Chem. Eng. Data* 61 (2016) 398–403.
- [38] T. Klein, S. Yan, J. Cui, J.W. Magee, K. Kroenlein, et al., Liquid viscosity and surface tension of n-hexane, n-octane, n-decane, and n-hexadecane up to 573 K by surface light scattering, *J. Chem. Eng. Data* 64 (2019) 4116–4131.
- [39] T. Klein, F.D. Lenahan, M. Kerscher, M.H. Rausch, I.G. Economou, et al., Characterization of long linear and branched alkanes and alcohols for temperatures up to 573.15 K by surface light scattering and molecular dynamics simulations, *J. Phys. Chem. B* 124 (2020) 4146–4163.
- [40] A. Krishnasamy, K.R. Bukkarapu, A comprehensive review of biodiesel property prediction models for combustion modeling studies, *Fuel* 302 (2021) 121085.
- [41] C. Li, Critical temperature estimation for simple mixtures, *Canadian J. Chem. Eng.* 49 (1971) 709–710.
- [42] N.S. Evangelista, F.R. do Carmo, H.B.J.I. de Sant'Ana, Estimation of physical constants of biodiesel-related fatty acid alkyl esters: normal boiling point, critical temperature, critical pressure, and acentric factor, *Ind. Eng. Chem. Res.* 57 (2018) 8552–8565.
- [43] S.J. Keasler, S.M. Charan, C.D. Wick, I.G. Economou, J.I. Siepmann, Transferable potentials for phase equilibria-united atom description of five- and six-membered cyclic alkanes and ethers, *J. Phys. Chem. B* 116 (2012) 11234–11246.
- [44] A. Ghoufi, P. Malfreyt, D.J. Tildesley, Computer modelling of the surface tension of the gas-liquid and liquid-liquid interface, *Chem. Soc. Rev.* 45 (2016) 1387–1409.
- [45] Q. Mao, A.C. van Duin, K.H. Luo, Formation of incipient soot particles from polycyclic aromatic hydrocarbons: A ReaxFF molecular dynamics study, *Carbon* 121 (2017) 380–388.
- [46] A.K. Agarwal, J.G. Gupta, A. Dhar, Potential and challenges for large-scale application of biodiesel in automotive sector, *Prog. Energy Combust. Sci.* 61 (2017) 113–149.
- [47] E.G. Giakoumis, C.D. Rakopoulos, A.M. Dimaratos, D.C. Rakopoulos, Exhaust emissions of diesel engines operating under transient conditions with biodiesel fuel blends, *Prog. Energy Combust. Sci.* 38 (2012) 691–715.
- [48] J. Bian, D. Guo, Y. Li, W. Cai, Y. Hua, et al., Homogeneous nucleation and condensation mechanism of methane gas: A molecular simulation perspective, *Energy* 249 (2022) 123610.
- [49] C. Liu, H. Wang, Binary Diffusion Coefficients of Polycyclic Aromatic Hydrocarbons: A Molecular Dynamics Study, 11th U S National Combustion 2019.
- [50] F. Müller-Plathe, A simple nonequilibrium molecular dynamics method for calculating the thermal conductivity, *J. Chem. Phys.* 106 (1997) 6082–6085.